ANATOMY OF A MERGER: A NUMERICAL MODEL OF A754

KURT ROETTIGER

Goddard Space Flight Center, Code 930, Greenbelt, MD 20771; kroettig@pecos1.gsfc.nasa.gov

JAMES M. STONE[1]

Department of Astronomy, University of Maryland, College Park, MD 20742-2421; jstone@astro.umd.edu

AND

RICHARD F. MUSHOTZKY

Goddard Space Flight Center, Code 662, Greenbelt, MD 20771; mushotzky@lheavx.gsfc.nasa.gov

ABSTRACT

A754 is a well-observed cluster of galaxies ($z = 0.054$) that exhibits a variety of morphological peculiarities. These include a bar of X-ray emission that is offset significantly from the galaxy distribution, an elongated X-ray surface brightness distribution extending between two distinct peaks in the galaxy distribution, and an extremely nonisothermal and asymmetric intracluster medium temperature morphology. Using these observational constraints, we present a numerical hydro/N-body model of A754 in which two clusters (2.5:1 mass ratio) have merged nearly in the plane of the sky less than 0.5 Gyr ago with an impact parameter of ~ 120 kpc and an impact velocity of ~ 2500 km s^{-1} (roughly the escape velocity of the primary cluster). Our models allow us to identify the origin of A754's peculiar X-ray and temperature morphologies, the underlying hydrodynamical processes that shape them, and their future evolution. We make detailed predictions for future high-resolution X-ray spectroscopic observations (e.g., *Astro-E*). We discuss general properties of our models that will be characteristic of off-axis mergers. In particular, we find significant nonthermal pressure support within the central region that could bias cluster mass estimates. We find significant angular momentum imparted on the gas distribution in the cluster. We find that mixing of the subcluster gas components is an inefficient process, particularly at large radii. Finally, we find that subsequent dark matter core passages result in an extended relaxation timescale.

Subject headings: galaxies: clusters: individual (A754) — galaxies: intergalactic medium — hydrodynamics — methods: numerical — X-rays: galaxies

1. INTRODUCTION

In recent years, clusters of galaxies have become essential cosmological probes. Both their current dynamical state and their internal structure provide important clues to conditions in the early universe. Over the years, many researchers (e.g., Geller & Beers 1982; Dressler & Shectman 1988; West & Bothun 1990; Jones & Forman 1991; Bird 1994; Davis 1994; Mohr et al. 1995; among others), using both X-ray and optical databases, have attempted to understand the dynamical state of clusters through analysis of their projected substructure (i.e., clumpiness and asymmetries in the distribution of the intracluster medium [ICM] and galaxies). Unfortunately, these studies are inherently limited because they represent only a two-dimensional projection of the true three-dimensional cluster shape and, moreover, there is no information regarding the gas kinematics. As such, the current data set cannot reveal the underlying physical processes that produce the observed substructure nor can they reveal how the substructure will evolve in time. For these answers, one must turn to numerical simulations (e.g., Evrard 1990; Cen 1992; Roettiger, Burns, & Loken 1993; Schindler & Müller 1993; Pearce, Thomas, & Couchman 1994; Navarro & White 1994; Mohr et al. 1995; among others). In this paper, we apply numerical hydrodynamical/N-body simulations to the analysis of the extensive observational database collected on the galaxy cluster Abell 754.

At $z = 0.054$, A754 is one of the most extensively observed clusters in both the optical and X-ray bands. Much attention has been drawn to this particular cluster by its peculiar X-ray morphology (Fabricant et al. 1986, hereafter F86; Henry & Briel 1995, hereafter HB95). Far from being a relaxed spherical distribution centered on the galaxies, A754 shows an elongated and barred X-ray morphology significantly offset from a bimodal galaxy distribution. Even more recently, A754 has been recognized for its significant nonisothermality (HB95; Henriksen & Markevitch 1996, hereafter HM96). Together, these properties make A754 an ideal laboratory for the study of nonequilibrium systems.

The purpose of this paper is to assemble the observational database on A754 and create a plausible, although not necessarily unique, self-consistent, numerical model that is in general agreement with the observational data. The model is then used to explore the underlying hydrodynamical processes that produced the observed morphological features, with particular emphasis on the X-ray surface brightness and temperature distribution. We then follow the development of these features as the merger is allowed to evolve, thus giving insight into the more general evolution of a slightly off-axis merger.

We perform this study using a hydrodynamical/N-body code based on the piecewise parabolic method (PPM) and a particle-mesh (PM) algorithm. The gaseous ICM (as represented by the PPM) is allowed to evolve self-consistently (including self-gravity) within a changing gravitational potential defined largely by the dark matter distribution as

represented by the collisionless N-body particles. In this study, we employ idealized initial conditions in a manner similar to previous studies by Roettiger et al. (1993), Roettiger, Burns, & Pinkney (1995), Roettiger, Burns, & Loken (1996), Roettiger, Loken, & Burn (1997a), Pearce et al. (1994), and Ricker (1997). The Pearce et al. simulations are based on a smoothed particle hydrodynamics code (Lucy 1977), while Ricker (1997) explores extremely off-axis mergers. The idealized initial conditions used here allow us to control explicitly the merger parameters, making possible a systematic survey of parameter space. It also allows for an efficient use of the computational volume, providing improved resolution over simulations of large-scale structure formation. On the other hand, our study is limited by the neglect of large-scale tidal forces, cosmological infall, and uncertainty in the detailed structure of clusters. The cosmological infall of baryonic matter is not likely to affect the inner regions of the cluster that are of interest here. Of potentially greater importance, these simulations do not include radiative cooling that may influence the cluster's thermal evolution, particularly in the high gas density core.

In § 2, we review the recent optical and X-ray observations of A754. In § 3, we describe the numerical method, the code, grid configuration, etc. In § 4, we discuss the degrees of freedom in the model and the manner in which the observations are used to constrain the model parameters. Here we also describe the initial conditions and summarize the merger parameters. In § 5, we make a quantitative comparison of our model with the observational data while discussing the current dynamical state of A754. In § 6, we describe the future evolution of the system. We summarize our results in § 7. We define $h = H_0/100$ for consistency with previous observational results, but we choose $H_0 = 65$ km s^{-1} Mpc^{-1} for the scaling of our model.

2. OBSERVATIONAL DATA

2.1. Optical Data

Many studies have been performed on the distribution of galaxies in A754. Of these, many have found significant substructure (e.g., Geller & Beers 1982; F86; Escalera & Mazure 1992, hereafter EM92; Bird 1994; Zabludoff & Zaritsky 1995, hereafter ZZ95) while others have not (e.g., Dressler & Shectman 1988; West & Bothun 1990). Of those studies that do find substructure, two primary galaxy concentrations are identified consistently. Their spatial location relative to the X-ray surface brightness distribution is indicated in Figure 1 (see also Plate L8 in ZZ95). Hereafter, we refer to these as the SE and NW concentrations. Table 1 is a
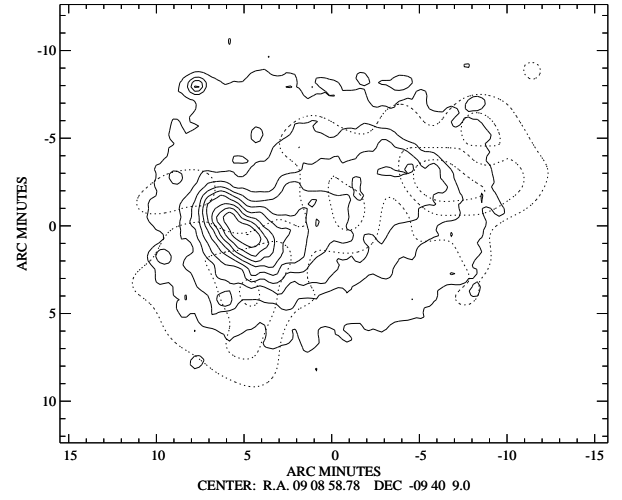

FIG. 1.—*ROSAT* X-ray surface brightness (*solid contours*) and projected galaxy density (*dotted contours*). The galaxy distribution is derived from F86 and Dressler & Shectman (1988). In all, 142 galaxy positions were smoothed with 2′.5 Gaussian. The X-ray surface brightness is smoothed with a 40″ Gaussian. Contours are at 0.08, 0.16, 0.24, 0.32, 0.4, 0.48, 0.56, 0.64, 0.72, 0.80, 0.90, and 0.99 of the peak.

summary of the individual subcluster properties as determined by several researchers.

Examination of Table 1 reveals a general consistency between the various analyses. The largest discrepancy resides in the velocity dispersion of the NW population determined by EM92. Their value differs from the other two by greater than 2 σ and is less than the dispersion calculated for the SE group. In each of the other two studies, the NW group has a larger velocity dispersion than the SE group. It is also interesting to note that in each study more galaxies are found to be associated with the SE subcluster than with the NW subcluster.

The various estimates of A754's virial mass are consistent, although uncertainties are large. Biviano et al. (1993) find $4.07^{+5.05}_{-2.23} \times 10^{14} M_\odot$ and $6.03^{+4.67}_{-2.65} \times 10^{14} M_\odot$ within 0.75 h^{-1} and 1.5 h^{-1} Mpc, respectively. Escalera et al. (1994) find $10.48 \pm 3.27 \times 10^{14} M_\odot$ corresponding to a virial radius of 2.21 ± 0.28 h^{-1} Mpc. Only EM92 have attempted to determine masses for the individual concentrations. They find $2.9 \times 10^{14} M_\odot$ and $1.3 \times 10^{14} M_\odot$ within ~ 0.32 Mpc for the SE and NW concentrations, respectively.

To summarize, the data are consistent with two clusters at nearly identical redshifts having a projected separation of 0.73 h^{-1} Mpc (ZZ95). Their velocity dispersions are of order 900 km s^{-1}, with the ratio of their dispersions consistent with unity. The total mass of the system within ~ 2 h^{-1}

TABLE 1

OBSERVED SUBCLUSTER GALAXY PARAMETERS

REFERENCE	v_r (km s^{-1}) SE[b]	v_r (km s^{-1}) NW[c]	σ_v (km s^{-1}) SE[b]	σ_v (km s^{-1}) NW[c]	N_g[a] SE[b]	N_g[a] NW[c]
F86	16145 ± 160	16165 ± 217	733^{+156}_{-102}	839^{+223}_{-132}	21	15
EM92......	16387	16007	698	521	12	10
ZZ95	16320 ± 132	16432 ± 191	830^{+130}_{-112}	970^{+156}_{-134}	41	27

[a] Number of galaxies associated with the subcluster.
[b] Southeastern subcluster.
[c] Northwestern subcluster.

Mpc, based on the galaxy dynamics, is likely greater than $10^{15} M_\odot$.

2.2. X-Ray Data

The *ROSAT* X-ray surface brightness image generated by HB95 reveals an unusually complex morphology. We have reproduced this data in Figure 1 (*solid contour*). There are several features worth noting: (1) the general elongation that extends parallel to the line connecting the galaxy concentrations (§ 2.1); (2) the peak of the X-ray distribution is seen to be a well-defined bar that extends up to $\sim 4'$ to the north of the SE galaxy concentration and is nearly perpendicular to the line connecting the galaxy concentrations. In a wavelet analysis of the X-ray surface brightness distribution (Slezak, Durret, & Gerbal 1994; Fig. 16 therein), the peak of the distribution is associated with an angled feature that includes the bar and a less well-defined extension toward the NW galaxy concentration. The total effect is that the eastern edge of the bar is sharper than the western edge. Finally, it is important to note that neither of the major galaxy concentrations are spatially coincident with the peak X-ray emission (ZZ95). The dominant galaxy in A754, identified as a cD galaxy (Dressler 1980), is located in the NW subcluster, 13' from the X-ray peak.

The mean temperature of the X-ray–emitting gas in A754 is 9 keV (HM96). Using the global velocity dispersion of 750 km s^{-1} (Mazure et al. 1996), $\beta = \mu m_h \sigma_v^2 / kT$ is found to be 0.4, which is significantly discrepant from the best-fit mean value of 0.94 ± 0.08 found by Lubin & Bahcall (1993) for a large sample of nearby clusters. In any case, the mean temperature may be misleading in that A754 is decidedly non-isothermal. Henriksen (1993), using *HEAO 1* A-2 data, identified two ill-defined temperature components within A754. HB95, using *ROSAT* data, were the first to produce a detailed temperature map of A754. They found a relatively cool region near the X-ray peak at ~ 5–7 keV. To the north and south, they identify arcs of gas greater than 9 and 10.8 keV, respectively. To the west, they identify an arc with temperature greater than 13.8 keV.

A similar attempt to map the temperature distribution was made by HM96 using *ASCA* data. Although differing in detail, there is considerable consistency between the HB95 and HM96 maps. Only one of the nine central regions (as defined by HM96; Fig. 1 therein) differed by a statistically significant amount from the corresponding region in HB95. Even in the low surface brightness outer regions of the cluster where the detailed energy dependence of the *ASCA* point-spread function and the background subtraction are both important, there is considerable agreement between the two maps. It is likely that much of the observed discrepancy results from the different energy bands employed. The low-energy *ROSAT* band (0.1–2.5 keV) is less able to constrain the temperatures of the extremely hot gas observed by *ASCA*, which is sensitive to the 0.5–10 keV band.

Finally, for completeness, we comment on the evidence for a cooling flow in A754. Edge, Stewart, & Fabian (1992) report evidence for a moderate cooling flow, $\sim 24 M_\odot$ yr^{-1}. However, there is no evidence for the optical filaments often associated with cooling flows (Heckman et al. 1989). Both HB95 and HM96 report relatively low temperatures (~ 6 keV) near the X-ray maximum. It has been suggested that this is cool gas having been stripped from one of the subclusters (HM96). It is also possible that this is a remnant of a cooling flow that was disrupted by the merger. No attempt was made to model a premerger cooling flow, although we would expect one to have been disrupted during the merger (Gómez et al. 1997). If there had been a long-established cooling flow in A754 before the merger, it is quite likely that remnant cool gas would remain at this early epoch of the merger owing to the inefficient mixing of cluster gas components (see § 6.3).

3. NUMERICAL METHOD

We compute the dynamical evolution of merging clusters of galaxies using a hybrid hydrodynamical/*N*-body code in which the hydrodynamical component is CMHOG, written by one of us (J. M. Stone). CMHOG solves the fluid equations using an implementation of the PPM (Colella & Woodward 1984) in its Lagrangian remap formulation: its fidelity has been demonstrated through numerous applications in interstellar gas dynamics, e.g., the interaction of strong shocks with dense clouds (Stone & Norman 1992). The collisionless dark matter is evolved using an *N*-body code based on a standard PM algorithm (Hockney & Eastwood 1988). The particles are evolved on the same grid as the gas using the same time step. The time step is determined by applying the Courant condition simultaneously to both the dark matter and the hydrodynamics. The only interaction between the collisionless particles and the gas is gravitational. Since we are modeling an isolated region, the boundary conditions for Poisson's equation are determined by a multipole expansion of the mass distribution contained within the grid (Jackson 1975). Particles that leave the grid are lost to the simulation. Typically, less than a few percent of the particles leave the grid. Previously, this code has been used to examine systematic errors in the measurement of the Hubble constant using the Sunyaev-Zeldovich effect in merging clusters of galaxies (Roettiger, Stone, & Mushotzky 1997b).

The simulation is fully three dimensional. Two different computational grids were used. A survey of parameter space was performed on the MasPar-2 at Goddard Space Flight Center using a fixed and rectangular grid ($256 \times 128 \times 128$ zones) having linear dimensions of $12.8 \times 8.3 \times 8.3$ Mpc. The merger axis coincides with the grid's major axis along which resolution is uniform and scales to 50 kpc, or ~ 5 zones per primary cluster core radius. Resolution along the grid's minor axis is uniform within the central 64 zones, and gradually decreases in the 32 zones on either side. That is, the resolution is a uniform 50 kpc extending 1.6 Mpc (32 zones) on either side of the major axis. Beyond 1.6 Mpc, the zone dimensions increase by $\sim 3\%$ from one zone to the next out to the edge of the grid. We use outflow boundary conditions for the hydrodynamical evolution. Once we settled on a set of initial conditions, we ran a very high resolution simulation on the CM-5 at the National Center for Supercomputing Applications using a fixed rectangular grid with dimensions of $512 \times 256 \times 256$, giving a resolution of 25 kpc in the central 3.2 Mpc (128 zones), or nearly 10 zones per core radius.

4. MODEL CONSTRAINTS

4.1. The Data and Its Limitations

We use the above observations to constrain our numerical model. However, there are serious limitations to this process. First, the observational uncertainties can be large.

Second, we believe, as did ZZ95, that this is a major merger in the very early stages after core passage. If this is the case, then the structure, temperature, and even the mass of the initial systems can be severely obscured by the current non-equilibrium conditions (Roettiger et al. 1996). Finally, there are just too many free and not necessarily independent parameters to completely constrain the model. These include the total mass of the system, the relative masses of the individual subclusters, the distribution of mass within the subclusters ($\rho \sim r^{-n}$, core sizes, etc.), the fraction of mass contained in baryons, the distribution of baryons relative to the dark matter (i.e., the β-parameter, central gas density), the angular momentum of the system (impact parameter and velocity), the linear scaling (we assume $H_0 = 65$ km s^{-1} Mpc^{-1}), the merger epoch (time since closest approach), and the orientation of the merger with respect to the observer. For these reasons, it is difficult to claim a definitive model. Rather, we have produced a model that agrees well enough with the observational data that we may consider it to be a plausible representation of the gasdynamics within A754.

Our approach is to use the observable properties of the general cluster population to construct our initial clusters. We then explore essentially two branches of parameter space (relative central gas density and impact parameter; § 4.3) at low resolution (50 kpc per grid zone), determine a best fit, and then run a high-resolution (25 kpc per grid zone) simulation, which is discussed in § 5

4.2. Initial Conditions

Since it is likely that much of the information about the internal structure of the premerger clusters has been erased by the merger, we begin with clusters that are consistent with observations of presumably relaxed systems. Both subclusters were chosen to have the same mass distribution. For our clusters, we have chosen the lowered isothermal King model described in Binney & Tremaine (1987). The lowered isothermal King model is a family of mass distributions characterized by the quantity ψ/σ^2 that essentially defines the concentration of matter. As ψ/σ^2 increases, the concentration parameter also increases, i.e., the core radius (r_c) decreases relative to the tidal radius (r_t). We have chosen a model with $\psi/\sigma^2 = 12$ in which we have truncated the density distribution at $15r_c$. Near the half-mass radius, the total mass density follows a power-law distribution, $\rho = r^{-\alpha}$, where $\alpha \sim 2.6$. This model is consistent with mass distributions produced by the cosmological N-body simulations of Crone, Evrard, & Richstone (1994) that showed $\alpha \sim 2.4$ in a high-density universe ($\Omega = 1$) and $\alpha \sim 2.9$ in a low-density universe ($\Omega = 0.2$). Observationally, galaxies are distributed as $\alpha \sim 2.4 \pm 0.2$ (Bahcall & Lubin 1994).

The simulations are conducted in scaled units. They are rescaled to meaningful physical dimensions after the fact. This gives us some flexibility in defining the initial conditions in that dimensionless subcluster parameters are more important than the global scaling. The observational data do give some insight into the scaling of global parameters. The various mass estimates listed in § 2.1 seem to indicate that the total mass within 2–3 Mpc is likely greater than $1.0 \times 10^{15} M_\odot$. The observed redshift of A754 indicates that the galaxy concentrations are separated by ~ 1.12 Mpc for $H_0 = 65$ km s^{-1} Mpc^{-1}.

The attempts to separate the two galaxy components can be used to constrain their relative masses. There is consider-

able uncertainty in doing so since, at this stage of the merger, the velocity dispersions may not be representative of the individual masses. We have found in previous (e.g., Roettiger et al. 1993) simulations that subclusters are "heated" relative to the primary as they pass through or near its core. Consequently, they may appear more massive than they actually are. Also, as seen in Table 1, small-number statistics lead to large uncertainties in the velocity dispersions. The ratio of the NW to SE subcluster velocity dispersions are consistent with unity, which would indicate that they are of comparable mass (assuming heating is not significant). Taken at face value, the velocity dispersions in F86 and ZZ95 indicate that the NW subcluster is somewhat more massive than the SE subcluster, while EM92 indicates that the SE subcluster is more massive. Looking at the galaxy counts in Table 1, and assuming that the galaxies trace the dark matter mass and that a significant exchange of galaxies has not occurred, all three samples in Table 1 indicate that the SE subcluster is the more massive subcluster. HB95 also suggests that the SE subcluster is the original main cluster based on its central location relative to the presumably undisturbed outer X-ray contours. For these reasons, we consider mergers where the SE subcluster is the more massive cluster by a factor of 2.5. Although marginally consistent with the velocity dispersions of F86 and ZZ95, it does represent one extreme, and a lower mass ratio (approaching 1:1) cannot be ruled out.

4.3. Parameter Space

Having settled on the relative cluster masses, we then explored a range of impact parameters and relative central gas densities. We examined impact parameters ranging from zero (head-on) to the sum of the respective core radii (Table 2). We found that in order to generate the combination of compression and shear necessary to produce the X-ray core morphology, the cores of the interacting clusters must overlap. Similarly, for a given total mass ratio, the relative ram pressure experienced by the clusters is determined by the relative central gas densities. The central gas density ratio (n_{eo1}/n_{eo2}) was varied from 0.5 to 2.0. The goal was to have enough ram pressure to create the desired X-ray core morphology but not so much that the subcluster penetrates the primary core.

The central gas densities are determined by a combination of the global gas fraction (f_b) and the distribution of the gas relative to the dark matter (i.e., the β-parameter). We do not attempt to determine the global gas fraction from the data. Rather, we arbitrarily choose the more massive cluster to have $f_b = 0.12$ and $\beta = 0.75$ (see § 2.2). Both values are within the acceptable range defined by observation (e.g., Jones & Forman 1984; White & Fabian 1995; Lubin & Bahcall 1993). We then varied these parameters for the less massive cluster, also within the observed range, in order to obtain the desired central gas density ratio.

Below we briefly summarize the initial cluster parameters. We further discuss the specific effects of parameter space in § 5.

4.4. A Brief Model Summary

Table 2 contains the initial cluster parameters. These clusters were allowed to merge under the influence of their mutual gravity. They are given an initial velocity of 270 km s^{-1} parallel to the line of centers and 100 km s^{-1} perpen-

TABLE 2

INITIAL CLUSTER PARAMETERS

Cluster Identification	M_{tot}[a] $(10^{14} M_\odot)$	T_e[b] (keV)	σ_v[c] (km s^{-1})	r_c[d] (kpc)	f_g[e]	β[f]	n_{eo}[g] $(10^{-3}$ cm$^{-3})$	v_{impact}[h] (km s^{-1})	Δr[i] (kpc)
1	8.0	6.7	785	220	0.12	0.75	1.55	2500	120
2	3.2	3.1	526	135	0.06	0.72	1.01	...	...

[a] Total mass $R < 3$ Mpc.
[b] Temperature.
[c] Velocity dispersion.
[d] Core radius.
[e] Global gas fraction, by mass.
[f] β-parameter.
[g] Central gas density.
[h] Impact velocity (dark matter).
[i] Impact parameter.

dicular. This results in a slightly off-axis merger with an impact parameter of ~ 120 kpc and a final impact velocity of 2700 km s^{-1}. Both of these values are relative to the respective centers of mass of each cluster. The simulation most closely resembles A754 at ~ 0.3 Gyr after closest approach. Although the relative masses of the two clusters are poorly constrained, it is important that the SE component (the primary cluster in our model) have the greater central gas density initially. It is also important that the NW component (secondary cluster in our model) have a relatively more concentrated mass distribution. Below we discuss the justification for the choice of these parameters.

5. A COMPARISON WITH THE DATA

Figure 2 (Plate 1) contains plots of four quantities overlaid with the X-ray surface brightness contours. They include (1) the projected, emission-weighted ICM temperature, (2) the dark matter distribution, (3) the gas velocity in the plane of the merger, and (4) a dynamically inert quantity used to trace the two gas components, also within a slice taken in the plane of the merger. In each case, the data are taken from the high-resolution simulation (see § 3), but it represents only a small fraction of the total volume (80 × 80 zones, in projection). The X-ray emissivity was calculated using the Mewe-Kaastra-Liedahl emission spectrum for optically thin plasmas supplied with XSPEC (Arnaud 1996). The X-ray surface brightness is simply a line-of-sight integration of the volume emissivity. Similarly, the emission-weighted, projected ICM temperature is simply a line-of-sight integration of the product of the temperature within a given zone and the X-ray emissivity in that same zone divided by the total emissivity along a given line of sight. The dark matter distribution is the projected particle density. The merger is assumed to be exactly in the

plane of the sky. The epoch depicted is 0.3 Gyr after the closest approach of the respective dark matter centers of mass. The smaller of the two clusters has moved left to right, passing below the core of the more massive cluster. Hereafter, we refer to the lower left dark matter concentration as the primary cluster, and to the upper right dark matter concentration as the subcluster. When comparing with the observational data, lower left is SE, upper right is NW. Table 3 shows a comparison of some of the global cluster parameters.

5.1. X-Ray Morphology and Hydrodynamics

The simulated X-ray surface brightness morphology at 0.3 Gyr is represented by contours in each of the four panels in Figure 2. Using our model, we are able to reproduce the basic features of A754's X-ray morphology (§ 2.2; Fig. 1). These include the bar-shaped peak in the X-ray emission, the displacement of the X-ray peak relative to the galaxies/dark matter, and the overall east-west elongation of the X-ray emission. The relationship between the orientation of the emission peak and the overall X-ray surface brightness distribution represents an isophotal twisting of nearly 90°. We now identify the underlying processes responsible for the morphological features exhibited by the simulated data.

The flattening of the X-ray peak on the eastern side is a result of the extreme ram pressure (ρv^2) of the subcluster on the primary. At the time of closest approach (as defined by the respective dark matter centers of mass), the relative velocity is ~ 2500 km s^{-1}. Since the merger is slightly off-axis, a portion of the subcluster (moving east to west) essentially runs into a wall of gas (i.e., the core of the primary cluster), with sufficient ram pressure to flatten the distribution and displace it relative to the dark matter. Figure 2c shows the basic flow pattern within a two-dimensional slice

TABLE 3

POSTMERGER COMPARISON

Data	N_g(SE)[a]	N_g(NW)[b]	σ_v(SE)[c] (km s^{-1})	σ_v(NW)[d] (km s^{-1})	$\langle T_e \rangle$[e] (keV)	M_{tot}[f] $(10^{14} M_\odot)$
Observed	41	27	830^{+130}_{-112}	970^{+156}_{-134}	9.0	10.48 ± 3.27
Simulated	50000	20000	1034 ± 105	830 ± 145	9.1	9.5

[a] Galaxy/particle count in SE subcluster (ZZ95).
[b] Galaxy/particle count in NW subcluster (ZZ95).
[c] Velocity dispersion in SE (ZZ95).
[d] Velocity dispersion in NW (ZZ95).
[e] Mean temperature (HM96).
[f] Total mass within ~ 2 Mpc (Escalera et al. 1994; virial mass).

in the plane of the merger. The maximum gas velocities at this epoch are associated with the residual infalling subcluster gas located SE of the X-ray peak. These gas velocities are seen to approach 1800 km s^{-1} (relative to the primary cluster dark matter distribution), but they abruptly decrease in magnitude ($<$1000 km s^{-1}) as they pass through a shock to the SE of the core after which the infalling gas is deflected by the core toward the SW and NE. Still, there is sufficient ram pressure to displace the X-ray peak from the gravitational potential minimum by a significant distance.

ZZ95 finds the peak of the X-ray emission to be displaced by 3$\farcs$8 from the peak of the SE galaxy concentration (assumed to be the minimum of the gravitational potential). Looking at the more statistically robust centroids of these distributions, the offset is somewhat less, $\sim$3$\farcs$0. Our model shows a dark matter/X-ray offset of 100 kpc that is $\sim$1$\farcs$5, assuming $H_0 = 65$ km s^{-1} Mpc^{-1}. Although somewhat less than the observed value, the simulated offset is in the same direction as that seen in the data and of comparable magnitude. A larger offset may be obtained by increasing the ram pressure of the secondary relative to the primary. However, if it is increased too much, the subcluster will actually penetrate the core of the primary and the barlike structure will be destroyed. Similarly, decreasing the impact parameter may also increase the offset.

Since the merger is slightly off-axis, a portion of the subcluster misses the primary core and meets with significantly less resistance as it passes to the south of the X-ray peak. Figure 2d shows the location of the respective gas components relative to the X-ray emission. The red indicates subcluster gas while black indicates primary cluster gas. In this analysis, we have used a dynamically inert quantity to trace the individual gas components within the velocity field. We find that the X-ray peak is composed almost entirely of gas originating with the primary cluster. The bulk of the subcluster gas is located SE of the X-ray peak. Very little mixing of the two components has occurred at this time. The leading edge of the subcluster gas appears as the westward extension of red. As the subcluster gas passes by the core, it creates a shear that drags both primary and subcluster gas into an extended tail along the bottom edge of the X-ray peak. The overall morphology of the remnant X-ray core is seen to have an angled or L-shaped distribution. This is reminiscent of a feature identified in the wavelet analysis of A754's X-ray surface brightness by Slezak et al. (1994; Fig. 16 therein). Along the interface between the two gas components, we note a spray of gas to both the NE and the SW, essentially perpendicular to the merger axis. The velocity of the spray is $\sim$1000 km s^{-1} near the X-ray peak but is seen to broaden and decelerate as it exits the core.

A comparison of the location of the subcluster gas component in Figure 2d with the location of the dark matter distribution in Figure 2b reveals that the subcluster gravitational potential (NW) has been completely stripped of its original gas content. A similar stripping was noted by Pearce et al. (1994). This is not to say that the remnant subcluster is devoid of gas. Rather, it drags along gas originally associated with the primary, causing it to interact strongly with gas infalling from the outer regions of the cluster. The interface between the expanding bow shock and the infalling gas is most noticeable in the temperature distribution (Fig. 2a; § 5.2) and in the gas velocity vectors (Fig. 2c), where a sharp transition is seen in the NW between gas

moving to the NW at up to 1000 km s^{-1} and gas moving to the SE at nearly 700 km s^{-1}. Regarding the X-ray morphology, it is the gas being dragged outward by the subcluster potential that accounts for the overall (SE to NW) elongation of the X-ray surface brightness. The implications for gas temperature morphology are discussed below (§ 5.2).

Of course, the gasdynamics in Figure 2c would not be directly observable since they are in the plane of the sky. In Figure 3, we show the line-of-sight gas velocities (vertical axis) in an east-west scan (horizontal axis) that intersects the X-ray surface brightness peak. That is, Figure 3 represents gas velocities in a plane perpendicular to the plane of the sky. A general expansion of the cluster gas is evident in this figure. The largest velocities ($\sim$1250 km s^{-1}) are in the region of the radial spray described above. We also see expansion velocities near 500 km s^{-1} in the region of the bow shock (right-hand side). These velocities should be resolved by Astro-E, provided the emissivity is great enough in the high-velocity regions. Of course, in an actual spectroscopic observation, the dynamical structure seen in Figure 3 would be projected along the line of sight and emission-weighted.

5.2. Temperature Distribution

Figure 2a shows the projected, emission-weighted temperature distribution (color) upon which the X-ray surface brightness distribution is superimposed (contours). The basic temperature morphology consists of two hot spots. The smaller, lower temperature hot spot located somewhat south and east of the X-ray peak is formed when residual gas from the subcluster collides with gas stalled near the
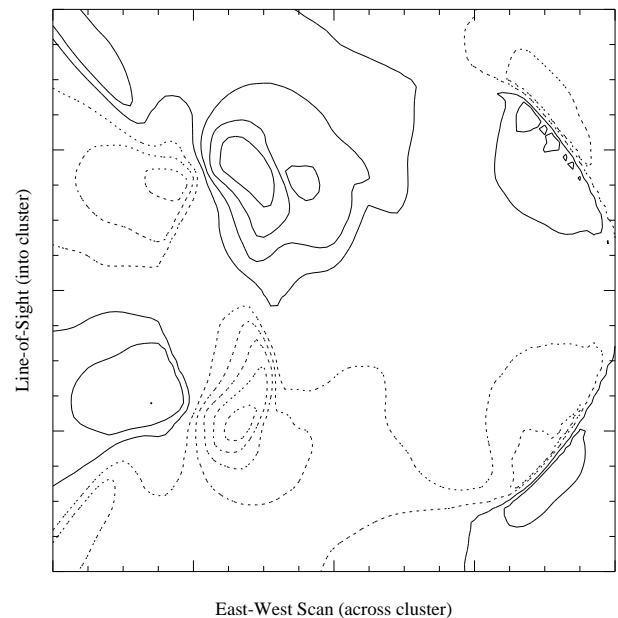

FIG. 3.—Line-of-sight gas velocities in an east-west scan that intersects the X-ray surface brightness peak. The vertical axis represents the observer's line of sight looking into the cluster. The horizontal axis represents an east-west scan across the projected face of the cluster. Contours are $\pm$250, $\pm$500, $\pm$750, $\pm$1000, and $\pm$1250 km s^{-1}. Negative velocities (approaching) are represented by dashed contours. Positive velocities (receding) are represented by solid contours. Tick marks represent 0.125 Mpc. The plot dimensions are the same as the panels in Fig. 2. In a spectroscopic observation of the cluster, the velocity structure seen in this figure would be emission-weighted and projected onto the plane of the sky. Consequently, much of the detailed structure may be unobservable.

X-ray peak. As such, this feature is not obviously apparent in the observational data, although it would be more consistent with the data if it were a somewhat lower temperature and/or farther S-SW. Our parameter-space survey shows it to be a strong function of both the relative gas content of the clusters and the impact parameter. Decreasing the gas content of the subcluster relative to the primary decreases the hot spot temperature relative to the surrounding gas by decreasing the ram pressure and limiting the residual infall. Decreasing the impact parameter moves the hot spot to the north and increases its temperature relative to the surrounding gas. Therefore, a better fit to the data may be possible by slightly increasing the impact parameter and decreasing the gas content of the subcluster. However, this must be balanced by other features. Specifically, we need sufficient gas in the subcluster to create the ram-pressure flattening and displacement of the X-ray peak (§ 5.1). This would argue for a more concentrated gas distribution in the subcluster.

The second hot spot appears as a large, slightly asymmetric arc near the western edge of the X-ray emission (Fig. 2a). The peak projected, emission-weighted temperature is greater than 19 keV and largely coincides with the subcluster dark matter distribution. As the subcluster impinges on the primary, a bow shock forms that produces a conical sheet of extremely hot gas. As the merger progresses, the shock-heated gas is driven through the primary. When viewed in projection, it appears as the arc that we see here. Although the subcluster is stripped of its initial gas content, the dark matter potential remains intact and drags a significant amount of primary cluster gas with it. This gas continues to interact with gas in the outer regions of the primary and helps to maintain the temperature of the original shock-heated gas. Coincident with the arc of hot gas is a discontinuity in the gas velocities that approaches 1700 km s^{-1}.

Another interesting temperature feature is the band of cooler gas (~ 7.5 keV) that runs along the X-ray peak. This is a combination of preshocked primary cluster gas (initially 6.7 keV) and subcluster gas that is deflected by the core and forced outward in the radial spray mentioned above (see § 5.1). As the spray expands and decelerates, the temperature drops to ~ 6.5 keV at 0.5 Mpc to the NE.

Figure 4 shows a quantitative point-by-point comparison of our model with the ASCA-based temperature map of A754 (HM96). Since we find a general consistency between the ASCA-based and ROSAT-based (HB95) temperature maps, we will only compare directly with the former. For the purposes of this analysis, we have placed a grid similar in scale and location (with respect to the X-ray emission) to the one used by HM96. Within each numbered region, we have calculated the mean projected, emission-weighted temperature in the model. We then compare these with the values observed in the corresponding regions. Error bars on the observed values are 90% confidence levels. Error bars on the model represent 1 σ about the mean. Data points have been slightly offset to minimize confusion. In each instance, the model is statistically consistent with the observed temperatures. The largest absolute discrepancy is found in region 7. We do find gas at ~ 19.5 keV in this region; however, because of the exact location of the grid, it becomes somewhat diluted with adjacent, cooler gas.

In these data, we recognize three basic features: (1) the negative gradient from region 1 to region 3; (2) the relatively
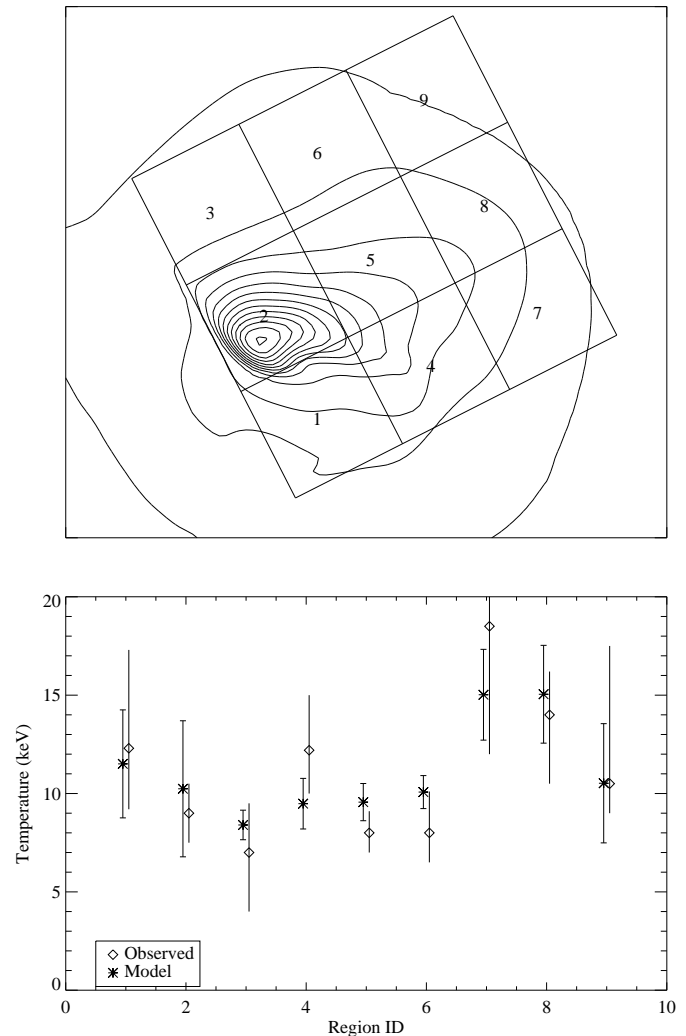

FIG. 4.—A comparison with the HM96 temperature map. *Top panel*: simulated X-ray surface brightness (*contours*) and grid similar in scale and location (relative to the X-ray image) to that used by HM96. *Bottom panel*: simulated, projected, emission-weighted temperatures (*asterisks*) within the numbered regions in the top panel compared directly with the corresponding temperatures observed by HM96 (*open diamonds*).

isothermal regions 4, 5, and 6; and (3) the negative gradient from region 7 to region 9. Each of these features is well represented in the model. The largest discrepancy is found in regions 4–6, where the model shows a slightly positive gradient and the data shows a somewhat stronger negative gradient because of the relatively hot region 4. Still, they are statistically consistent. As was suggested above, better agreement in region 4 might be obtained if the hot spot near the X-ray peak (Fig. 2c) were farther S-SW.

Of course, the X-ray telescope only allows us to see the projected, emission-weighted temperature. In doing so, much of the detailed structure and extremes in temperature can be hidden. Figure 5 shows the zone-by-zone distribution of the true (i.e., nonemission-weighted) model gas temperatures within a cube comparable in dimension to that delineated by the nine regions in Figure 4. Note the wide range in temperatures (5–22 keV). Although the bulk of the volume is dominated by gas less than 10 keV, the distribution is strongly skewed toward higher temperatures. Fully 29% of the volume is in gas greater than 11 keV. The
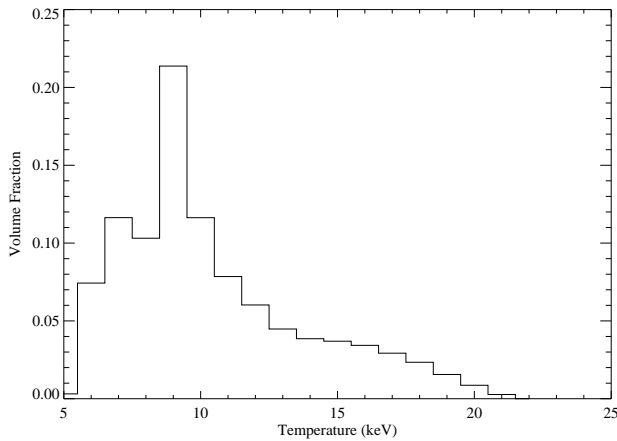
FIG. 5.—A histogram showing the zone-by-zone distribution of temperatures within the volume delineated by the nine regions in Fig. 4

median temperature is 9.9 keV, and the mean temperature is 10.9 keV. Let us compare these values to the mean emission-weighted temperature of 9 keV and the initial primary cluster temperature of 6.7 keV.

6. FUTURE EVOLUTION

Figures 6 and 7 (Plates 2 and 3) depict the model evolution at 2.75 and 5.25 Gyr after closest approach. These are the same quantities represented in Figure 2 ($T = 0.3$ Gyr) and therefore can be compared directly. Considerable evolution is evident. The subcluster dark matter distribution has proved to be rather resilient; not only does it survive the initial passage, but a couple of others as well. Through examination of the particle group velocities, we identify subsequent merger events at 1.6 and 2.5 Gyr. Although far less dramatic than the initial merger, these events are still significant in that they continually stir the ICM, preventing a rapid relaxation. At 2.75 Gyr, the system is experiencing a maximum separation that results in the peanut-shaped morphology of the dark matter distribution seen in Figure 6b (color). It should be noted that survival of substructure in the dark matter will depend on the relative masses of the subclusters as well as their relative concentration. As the mass ratio decreases (approaching 1:1), the subcluster will survive longer. Also, chances of survival will be enhanced as the subcluster mass distribution becomes more concentrated and as the impact parameter increases.

The continued dynamical evolution is still apparent in the X-ray surface brightness morphology (all four panels in Fig. 6). Although considerably more symmetric (i.e., relaxed) than during the epoch we find most consistent with A754, there is still a significant extension to the SE that is abruptly flattened. A comparison with the velocity vectors in Figure 6c indicates that the extension results from a southerly flow of ~ 650 km s^{-1}. The flattening occurs in a region of strong shear where the southerly flow is abruptly cutoff by a W-SW flow of ~ 700 km s^{-1}. In fact, the W-SW flow is part of a more global circulation that is seen to extend unbroken (at least in the plane of the merger) around the entire cluster. In this sense, the region of shear described above is the location where the flow meets itself. One by-product of the global circulation is the mixing of the subcluster and primary cluster gas components. Figure 6d demonstrates how the global circulation has drawn the sub-

cluster gas (red) around the remnant core. We examine the rate of gas mixing more quantitatively in § 6.3. Finally, the temperature extremes seen in A754 have been reduced significantly by 2.75 Gyr (Fig. 6a). At this time, the cluster would be considered largely isothermal, at least within the central region. To the NW, we find large regions of relatively cool gas (<6 keV) that are likely remnants from the initial merger. Although radiative cooling was not included in these simulations, we do find regions where the gas cools via adiabatic expansion, such as behind the initial bow shock.

Between 2.75 and 5.25 Gyr, there continues to be minor "sloshing" within the gravitational potential. The relative dark matter, center of mass velocities peak at only 100 km s^{-1}. At 5.25 Gyr, the X-ray surface brightness morphology is quite regular, with a slight elongation from the SE to the NW (Fig. 7). A similarly relaxed dark matter distribution is apparent in Figure 7b (color). Here the dark matter distribution appears somewhat more elongated than the gas distribution. Like the gas distribution, the dark matter major axis is oriented SE to NW, reflecting the axis of the secondary mergers. Unlike the gas distribution, the dark matter can shed angular momentum through free-streaming particles. Consequently, the secondary mergers discussed above are largely head-on.

Although temperature inhomogeneities persist, the overall temperature distribution is noticeably more regular (Fig. 7) than at earlier epochs. The cool regions noted at 2.75 Gyr have vanished while a radial temperature gradient peaking at 11 keV in the core has developed. Pearce et al. (1994) also note a centrally peaked temperature distribution. The relative heating in the core results from the continual stirring of the relatively high density gas in the core by fluctuations in the gravitational potential minimum as particles continue to stream back and forth along the merger axis. In the absence of radiative cooling, there is no way to dissipate the heat. We also find that the region NW of the cluster core is somewhat warmer (~ 1–2 keV) than the corresponding region to the SE. The overall temperature morphology at this time is similar to that of Triangulum Australis (Markevitch, Sarazin, & Irwin 1996).

Large-scale gasdynamics (both bulk flows and rotation) persist even as late as 5.25 Gyr. A general counterclockwise circulation in the merger plane is still evident by the velocity vectors in Figure 7c. Comparing with Figure 6c, we note that the flow is less coherent and of significantly reduced magnitude. The highest velocity gas (~ 850 km s^{-1}) is located in the extreme SE corner of Figure 7c. Within the central cluster, gas velocities range up to 600 km s^{-1}, but the average is nearer 300 km s^{-1}. As mentioned above, the gas is less efficient than the dark matter at shedding angular momentum. Over time, angular momentum is transferred via mixing to adjacent gas components. Similarly, kinetic energy is transferred from one component to the next and ultimately converted into heat. The relative inefficiency of this process is similarly apparent in the slow rate of mixing between primary and subcluster gas components, particularly in the outer regions of the merger remnant (Fig. 7d). We address mixing in more detail in § 6.3.

6.1. Evolution of Dynamical Pressure Support

Since dynamical information regarding the X-ray–emitting gas is nonexistent at this time, the analysis of clusters has always assumed them to be thermally supported

(i.e., in hydrostatic equilibrium). Several recent cluster analyses have argued for additional pressure components (e.g., dynamical, magnetic fields) in order to explain the apparent discrepancies between X-ray, virial, and gravitational lensing–based cluster mass estimates (e.g., Loeb & Mao 1994, among others). Using our model of A754, we can determine the relative significance of dynamical pressure support throughout the merger evolution.

Figure 8 shows the evolution of P_K/P_T ($P_K = \rho v^2$ and $P_T = kT$) within spherical volumes ($r = 0.4$ and 1.5 Mpc) centered on the gravitational potential minimum. Initially, the dynamical pressure is negligible, although it grows steadily as the subcluster impinges on the primary. A maximum is reached shortly before closest approach ($T = 0$), when the dynamical pressure is greater than 60% of the thermal pressure within 0.4 Mpc. Secondary maxima occurring near 2 and 3 Gyr correspond to subsequent passages by the subcluster dark matter remnant. As might be expected, the larger volume ($r = 1.5$ Mpc) experiences fewer extremes than the core, which may explain the relative heating in the core. After the initial impact, the dynamical pressure is typically $\sim 20\%$ of the thermal pressure but decays to 5%–10% after 4.5 Gyr. Therefore, late in the merger evolution, gasdynamics play a limited role in supporting the expanded gas core. This is consistent with Pearce et al. (1994).

Figure 8 has implications for X-ray–based cluster mass estimates. Neglecting the dynamical component of the pressure support will cause an underestimation of the cluster mass by a fraction $1 - [1 + (P_K/P_T)]^{-1}$. Based on this analysis, we would predict errors of $\sim 20\%$–40% or more during the 2 Gyr immediately after a merger and errors of 10%–20% at later times. Note also the radial dependence. Mass estimates based on only the central regions of the cluster will be more severely affected. These results are consistent, at least in magnitude, with previous studies (e.g., Evrard, Metzler, & Navarro 1996; Schindler 1996; Roettiger et al. 1996), although none of these studies show evidence for systematic underestimation of the cluster masses, indicating that other effects (e.g., projection effects) and the details of the observational analysis are also important. By underestimating the total mass, the baryon fraction

would be overestimated by the same factor. Although significant, the errors noted here are not enough to account for the apparent inconsistency between measurements of the baryon fraction in clusters and that derived from primordial nucleosynthesis models that assume $\Omega = 1$ (White et al. 1993). Of course, lowering the assumed value of Ω also reduces the perceived discrepancy.

6.2. Angular Momentum Evolution

The off-axis merger imparts considerable and sustained angular momentum upon the gas distribution in the merger remnant (Fig. 7). Although the gas distribution is not rotationally supported, it is slightly less prolate than the dark matter distribution where angular momentum is dissipated more readily by free-streaming particles. Figure 9 shows the evolution of total angular momentum density (L_{tot}) within concentric spheres of radius 0.4 and 1.5 Mpc centered on the gravitational potential minimum. We define $L_{tot} = [\sum_i^3 (L_i)^2]^{0.5}/N_z$ and $L_i = \sum_j^{N_z} (r_j \rho_j v_j)_i$ where r_j is the distance from the potential minimum to the jth zone, ρ_j and v_j are the gas density and velocity, respectively, within the jth zone, and N_z is the number of zones within the volume. The sum over i represents the sum over the Cartesian coordinates.

The angular momentum evolution in Figure 9 closely mimics the evolution of the nonthermal pressure support (see § 6.1; Fig. 8). The abrupt rise at $T = 0$ ($R < 0.4$ Mpc) occurs as the subcluster passes near the primary core. The subsequent decay occurs as the subcluster leaves the sphere only to return at 1.5–2.0 Gyr. Beginning at ~ 3.5 Gyr, the angular momentum within 0.4 Mpc is seen to decay steadily as the core relaxes and angular momentum is transferred via mixing to larger radii. Within the larger volume, the total angular momentum remains fairly constant, peaking slightly at 1.5–2.0 Gyr. Once again, this shows that, although the canonical core sound crossing time (and therefore its relaxation time) is of order 1 Gyr, true relaxation of the merger remnant does not really begin until after ~ 3 Gyr. The longer relaxation time is important to the interpretation of substructure frequency. A longer relaxation time allows for greater consistency between a high-
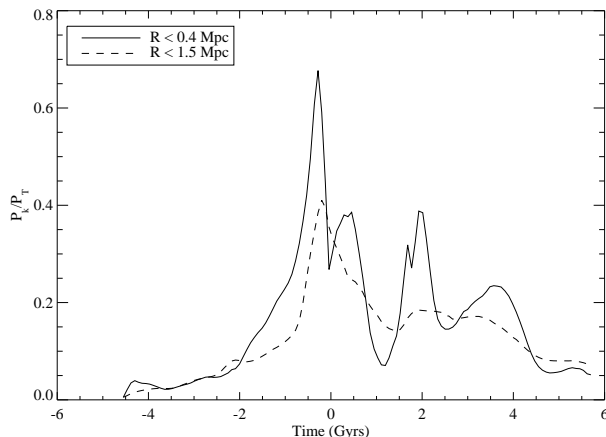

FIG. 8.—The evolution of the ratio of dynamical to thermal pressure support within spheres of radius 0.4 Mpc (*solid line*) and 1.5 Mpc (*dashed line*) centered on the gravitational potential minimum. The times are relative to the time of closest approach. This analysis was performed on the low-resolution simulation (§ 3).
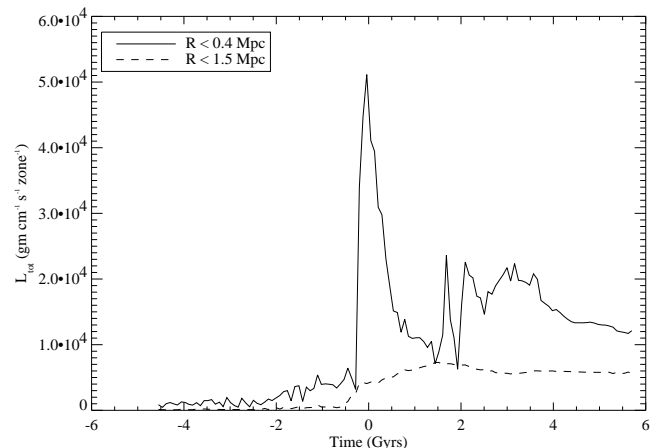
FIG. 9.—The evolution of the angular momentum density per zone relative to the gravitational potential minimum within spheres of radius 0.4 Mpc (*solid line*) and 1.5 Mpc (*dashed line*) centered on the potential minimum. The times are relative to the time of closest approach. This analysis was performed on the low-resolution simulation (§ 3).

substructure frequency and a low Ω, the density of the universe relative to the critical density (Boute & Xu 1997).

6.3. *Mixing*

Using a dynamically inert quantity evolved within the velocity field, we have traced the rate at which the primary and subcluster gas components mix. In addition to the non-isothermal temperature distributions observed in some clusters, Arnaud et al. (1994) have also noted an inhomogeneous abundance distribution in Perseus. Since considerable scatter is observed in global cluster abundances (Mushotzky & Loewenstein 1997), it may be reasonable to expect inhomogeneous distributions within individual clusters to arise as a result of mergers between clusters of differing initial abundances. It then becomes important to quantitatively assess the rate at which the remnant gas distribution becomes homogeneous. A cursory examination of Figures 2d, 6d, and 7d indicates that mixing is slow in any case, but even more so at larger radii where the gas-dynamics are less extreme. Even after 5.25 Gyr, there is a noticeable patchiness in the gas distribution. This result may be sensitive to cosmological infall, which we do not simulate.

Figure 10 presents the degree of mixing within spheres of radius 0.4 and 1.5 Mpc. The fraction of zones within the corresponding volumes that are at least 10% mixed is plotted. Mixing does not begin until after the time of closest approach ($T = 0$), at which point the degree of mixing within both 0.4 and 1.5 Mpc increases steadily with time. The level of mixing is consistently lower in the larger volume, although the rate of mixing within the two volumes track well until about 3–4 Gyr after the initial passage. At this time, mixing within the 1.5 Mpc sphere effectively stops while the rate of mixing within 0.4 Mpc actually increases. Let us recall from § 6.2 that it is at 3.5 Gyr when the ordered circulation in the core gives way to random motions, thus increasing the mixing efficiency. After 5 Gyr, 90% of the zones within 0.4 Mpc are at least 10% mixed, which compares with only 45% within the larger volume. This analysis would seem to indicate (1) a tendency to find more homogeneous gas distributions within the cores of clusters, (2) the potential for abundance gradients within clusters having
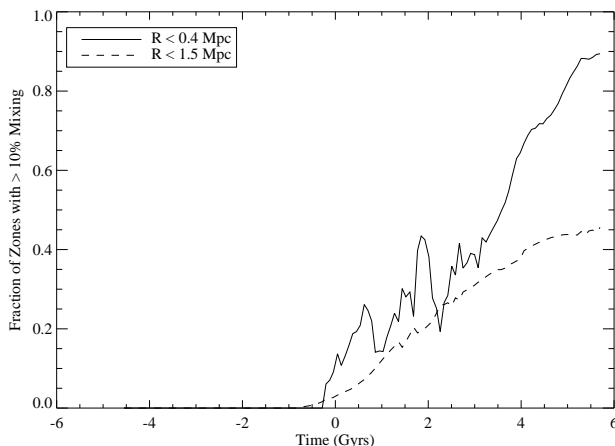
evolved sufficiently since their last significant merger, and (3) the potential for patchiness in the distribution of metals in the outer regions of clusters. Of course, patchiness may also result from a local enhancement of metals by supernovae in individual galaxies.

7. SUMMARY

We have presented a dynamical three-dimensional model of A754 that can explain many of its observed morphological peculiarities. In our model, A754 is the result of a very recent (<0.3 Gyr), nearly in the plane-of-the-sky merger between two clusters having a total mass ratio that is likely less than 2.5:1. The merger is slightly off-axis, with an impact parameter of 120 kpc or about half the initial primary cluster core radius. The final impact velocity is ~ 2500 km s^{-1}. Although the model is poorly constrained by the limited observational data, our assumed initial conditions for the merger are consistent with that data. The fact that the observed characteristics of A754 can be reproduced so well suggests that the actual properties of the merging clusters in A754 cannot be too different from those adopted here. Moreover, we believe that the dynamics described here are largely representative of slightly off-axis mergers.

In general, the results of these simulations are consistent with other studies of major cluster mergers (Roettiger et al. 1993, 1996, 1997a; Schindler & Müller 1993; Pearce et al. 1994). In particular, they reveal how gravitational energy is transferred to the ICM and dissipated via shocks, resulting in a heating and expansion of the ICM relative to that of the dark matter, and high-velocity bulk flows within the gas. It should be noted, however, that in this study, as well as many others, potentially important physical processes (e.g., radiative cooling, thermal conduction, magnetic fields, etc.) have been ignored. Moreover, we study the merger of isolated subclusters in hydrostatic equilibrium rather than mergers within an evolving large-scale structure. On the other hand, this allows us to focus our numerical resources on the dynamics of the merger itself. In addition, we are able to identify and analyze systematically the physical processes that govern the dynamics during mergers. Thus, our results have important implications for the dynamics of off-axis mergers in general.

More specifically, the main conclusions of this study include the following:

1. Major merger events can account for many if not all of the morphological irregularities observed in A754 as well as other well-resolved clusters. The extreme temperature inhomogeneities of the type observed in A754 are currently the most direct indicator of recent dynamical evolution and are particularly useful for ruling out more subtle projection effects. The simple projection of two clusters along a common line of sight cannot account for the sharp temperature transitions, due to shocks, nor the extreme nature of the observed temperatures (19 keV).

2. Relaxation of the merger remnant is delayed beyond the canonical sound crossing time by subsequent passages of the subcluster's remnant dark matter. The extended relaxation time allows for greater consistency between a high frequency of substructure in clusters of galaxies and a low-Ω universe (Buote & Xu 1997).

3. Major merger events can result in significant nonthermal pressure support within the remnant gas distribution. The existence of a nonthermal pressure component

FIG. 10.—The fraction of zones within spheres of radius 0.4 Mpc (*solid line*) and 1.5 Mpc (*dashed line*) centered on the gravitational potential minimum that exhibit at least 10% mixing. That is, the gas within that zone consists of at most 90% of either primary or subcluster gas. This analysis was performed on the low-resolution simulation (§ 3).

may seriously affect X-ray–based cluster mass estimates that often employ the assumption of hydrostatic equilibrium. Errors are lower when the mass estimates are made at larger radii, but they can still approach 30% within 1.5 Mpc during the early stages of a merger. At later times, errors are more typically 15%. These results are consistent in magnitude with Evrard et al. (1996) and Schindler (1996).

4. Off-axis mergers can impart significant angular momentum onto the remnant gas distribution resulting in a sustained rotation about the cluster core. The magnitude of rotation (and bulk flows) seen in this model should be observable with *Astro-E*. Although much of the gasdynamics in the A754 merger are not directly observable since they occur in the plane of the sky, we do predict that a general expansion of the cluster ICM may be observable, provided the emissivity of the high-velocity gas is great enough (see § 5.1). Since the time period between major mergers is likely comparable to or less than the observed relaxation timescales, the gasdynamics within the cluster may largely reflect those imparted by the last major merger.

5. Mixing of premerger gas components is an inefficient process and may explain the observed patchiness and gradients in both temperature and abundance distributions (e.g., Perseus [Arnaud et al. 1994] and Coma [Honda et al. 1996]). Mixing is most efficient in the core of the cluster where the gasdynamics are most significant.

REFERENCES

Arnaud, K. A. 1996, in ASP Conf. Ser. 101, Astronomical Data Analysis Software and Systems, ed. G. H. Jacoby & J. Barnes (San Francisco: ASP), 17
Arnaud, K. A., et al. 1994, ApJ, 436, L67
Bahcall, N., & Lubin, L. 1994, ApJ, 426, 513
Binney, J., & Tremaine, S. 1987, Galactic Dynamics (Princeton: Princeton Univ. Press)
Bird, C. 1994, AJ, 107, 1637
Biviano, A., Girardi, M., Giuricin, G., Mardirossian, F., & Mezzetti, M. 1993, ApJ, 411, L13
Boute, D. A., & Xu, G. 1997, MNRAS, 284, 439
Cen, R. 1992, ApJS, 78, 341
Colella, P., & Woodward, P. 1984, J. Comput. Phys., 54, 174
Crone, M. M., Evrard, A. E., & Richstone, D. O. 1994, ApJ, 434, 402
Davis, D. 1994, Ph.D. thesis, Univ. Maryland
Dressler, A. 1980, ApJS, 42, 565
Dressler, A., & Shectman, S. 1988, AJ, 95, 985
Edge, A. C., Stewart, G. C., & Fabian, A. C. 1992, MNRAS, 258, 177
Escalera, E., Biviano, A., Girardi, M., Giuricin, G., Mardirossian, F., Mazure, A., & Mezzetti, M. 1994, ApJ, 423, 539
Escalera, E., & Mazure, A. 1992, ApJ, 388, 23 (EM92)
Evrard, A. E. 1990, ApJ, 363, 349
Evrard, A. E., Metzler, C. A., & Navarro, J. F. 1996, ApJ, 469, 494
Fabricant, D., Beers, T. C., Geller, M. J., Gorenstein, P., Huchra, J. P., & Kurtz, M. J. 1986, ApJ, 308, 530 (F86)
Geller, M., & Beers, T. C. 1982, PASP, 94, 421
Gómez, P., Loken, C., Burns, J. O., & Roettiger, K. 1997, in preparation
Heckman, T., Baum, S., Van Breugel, W., & McCarthy, P. 1989, ApJ, 338, 48
Henriksen, M. J. 1993, ApJ, 414, L5
Henriksen, M. J., & Markevitch, M. L. 1996, ApJ, 466, L79 (HM96)
Henry, J., & Briel, U. 1995, ApJ, 443, L9 (HB95)

Hockney, R. W., & Eastwood, J. W. 1988, Computer Simulations Using Particles (Philadelphia: IOP)
Honda, H., et al. 1996, ApJ, 473, L71
Jackson, J. D. 1975, Classical Electrodynamics (New York: Wiley)
Jones, C., & Forman, W. 1984, ApJ, 276, 38
————. 1991, BAAS, 23, 1338
Loeb, A., & Mao, S. 1994, ApJ, 435, L109
Lubin, L., & Bahcall, N. 1993, ApJ, 415, L17
Lucy, L. B. 1977, AJ, 82, 1013
Markevitch, M., Sarazin, C. L., & Irwin, J. A. 1996, ApJ, 472, L17
Mazure, A., et al. 1996, A&A, 311, 95
Mohr, J. J., Evrard, A., Fabricant, D. G., & Geller, M. J. 1995, ApJ, 447, 8
Mushotzky, R. F., & Loewenstein, M. 1997, ApJ, 481, L63
Navarro, J. F., & White, S. D. M. 1994, MNRAS, 267, 401
Pearce, F. R., Thomas, P. A., & Couchman, H. M. P. 1994, MNRAS, 268, 953
Ricker, P. M. 1997, preprint
Roettiger, K., Burns, J. O., & Loken, C. 1993, ApJ, 407, L53
————. 1996, ApJ, 473, 651
Roettiger, K., Burns, J. O., & Pinkney, J. 1995, ApJ, 453, 634
Roettiger, K., Loken, C., & Burn, J. O. 1997a, ApJS, 109, 307
Roettiger, K., Stone, J. M., & Mushotzky, R. F. 1997b, ApJ, 482, 588
Schindler, S. 1996, A&A, 305, 858
Schindler, S., & Müller, E. 1993, A&A, 272, 137
Slezak, E., Durret, F., & Gerbal, D. 1994, AJ, 108, 1996
Stone, J. M., & Norman, M. 1992, ApJ, 390, L17
West, M. J., & Bothun, G. D. 1990, ApJ, 350, 36
White, D. A., & Fabian, A. C. 1995, MNRAS, 273, 72
White, S. D. M., Navarro, J. F., Evrard, A. E., & Frenk, C. S. 1993, Nature, 366, 429
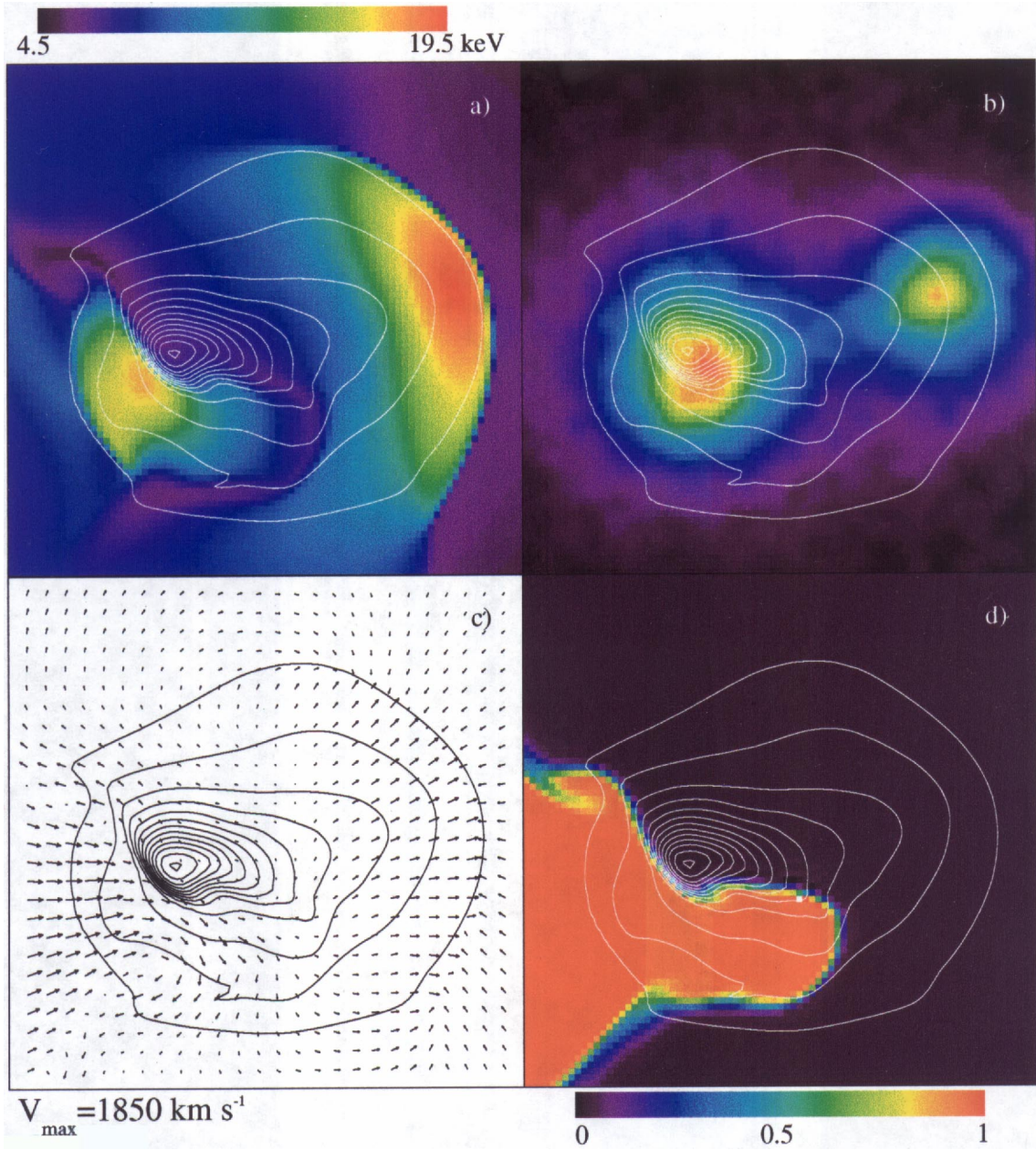Zabludoff, A. L., & Zaritsky, D. 1995, ApJ, 447, L21 (ZZ95)

Fig. 2.—Simulated data at 0.3 Gyr after closest approach. Each panel is 2 Mpc × 2 Mpc. The smaller of the two clusters (subcluster) entered from the left and is moving to the right. (a) X-ray surface brightness (contours) and projected emission-weighted temperature (color). Note the color bar above the panel. (b) Projected dark matter particle distribution (color). (c) Gas velocity within the plane of the merger. Vectors are spaced at 75 kpc (one-third the resolution of the simulation) and scaled to the maximum velocity indicated below the panel. (d) A dynamically inert quantity used to trace the subcluster gas component (red) as it mixes with the primary gas (black). Intermediate colors indicate the degree of mixing as shown in the color bar below the panel. The X-ray contours are at 0.03, 0.08, 0.16, 0.24, 0.32, 0.4, 0.48, 0.56, 0.64, 0.72, 0.80, 0.90, and 0.99 of the peak. These are the same as in Fig. 1, with the exception of the lowest contour.
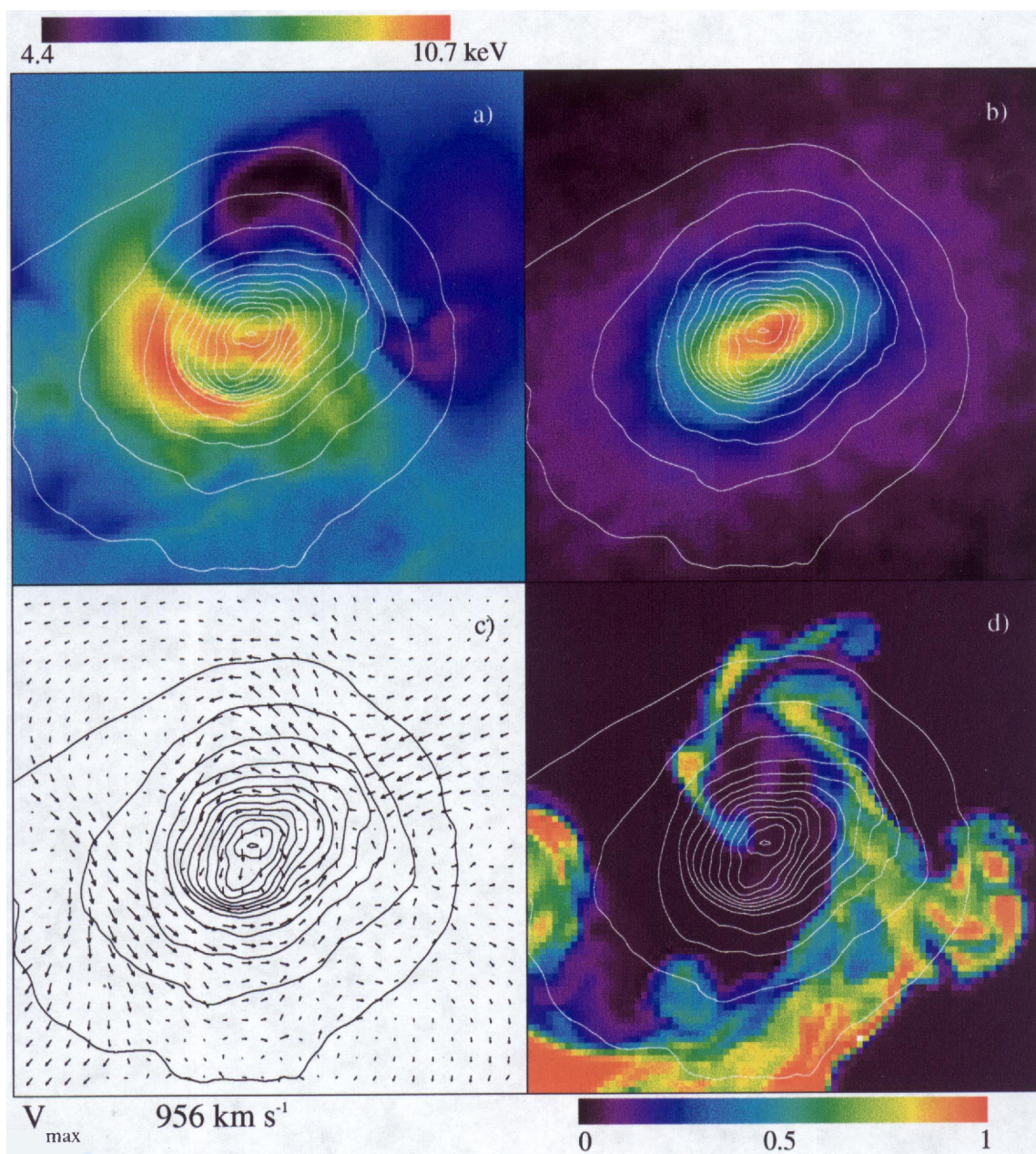
ROETTIGER, STONE, & MUSHOTZKY (see 493, 66)

PLATE 1

FIG. 6.—Same as Fig. 2, only at 2.75 Gyr after closest approach

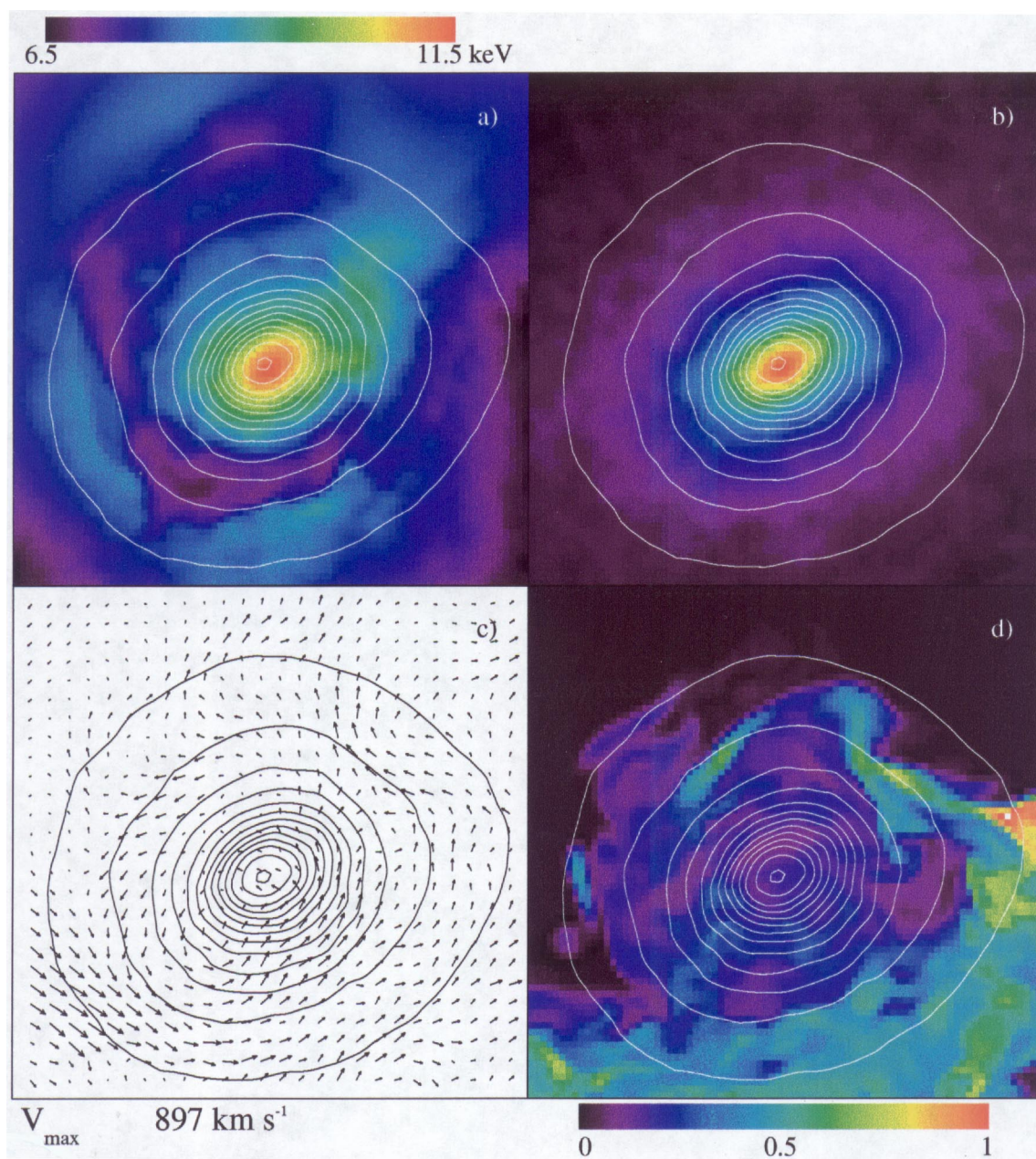ROETTIGER, STONE, & MUSHOTZKY (see 493, 69)

PLATE 2

Fig. 7.—Same as Fig. 2, only at 5.25 Gyr after closest approach

Roettiger, Stone, & Mushotzky (see 493, 69)

PLATE 3